Structure of mycobacterial cytochrome *bcc* in complex with Q203 and TB47, two anti-TB drug candidates

Shan Zhou[1,2,7], Weiwei Wang[3,7], Xiaoting Zhou[3], Yuying Zhang[2], Yuezheng Lai[2], Yanting Tang[2], Jinxu Xu[2], Xiaolin Yang[3], Luke W. Guddat[4], Quan Wang[3], Yan Gao[3*], Zihe Rao[1,2,3,5,6*] & Hongri Gong[2*]

[1]State Key Laboratory of Medicinal Chemical Biology, College of Pharmacy, Nankai University, Tianjin 300350, China

[2]State Key Laboratory of Medicinal Chemical Biology, College of Life Sciences, Nankai University, Tianjin 300071, China

[3]Shanghai Institute for Advanced Immunochemical Studies and School of Life Science and Technology, ShanghaiTech University, Shanghai 201210, China

[4]School of Chemistry and Molecular Biosciences, The University of Queensland, Brisbane, 4072 Queensland, Australia

[5]National Laboratory of Biomacromolecules, CAS Center for Excellence in Biomacromolecules, Institute of Biophysics, CAS, Beijing 100101, China

[6]Laboratory of Structural Biology, Tsinghua University, Beijing 100084, China

[7]These authors contributed equally

* Email: gaoyan04092020@163.com (Y.G), raozh@tsinghua.edu.cn (Z.R.), gonghr@nankai.edu.cn (H.G.).

Abstract

Pathogenic mycobacteria pose a sustained threat to global human health. Recently, cytochrome *bcc* complexes have gained interest as targets for antibiotic drug development. However, there is

currently no structural information for the cytochrome *bcc* complex from these pathogenic mycobacteria. Here, we report the structures of *M. tuberculosis* cytochrome *bcc* alone (2.68 Å resolution) and in complex with clinical drug candidates Q203 (2.67 Å resolution) and TB47 (2.93 Å resolution) determined by single-particle cryo-electron microscopy. *M. tuberculosis* cytochrome *bcc* forms a dimeric assembly with endogenous menaquinone/menaquinol bound at the quinone/quinol binding pockets. Q203 and TB47 are bound to the quinol-binding site. Hydrogen bonds are formed between the inhibitor and the side chains of $_{QcrB}$Thr313 and $_{QcrB}$Glu314, residues that are conserved across pathogenic mycobacteria. These high-resolution structures provide a basis for the design of new mycobacterial cytochrome *bcc* inhibitors that could be developed into broad spectrum drugs to treat mycobacterial infections.

Introduction

Mycobacteria, which belong to the phylum Actinobacteria, have coevolved with humans over thousands of years (Chisholm et al., 2016). Approximately 200 species of mycobacteria have been identified that have diverse lifestyles, morphologies, biochemistries and physiologies (Tortoli et al., 2017). Mycobacteria can broadly be grouped into two categories: tuberculosis-causing mycobacteria and non-tuberculous mycobacteria (NTM). *Mycobacterium leprae* is often represented in a distinct genetic clade owing to its genetic and phenotypic differences compared to other mycobacterium species (Cole et al., 2001). Mycobacteria can be further classified into fast-growing and slow-growing species or species complexes, these assignments are according to the physiological, phenotypic and phylogenetic characteristics (Rastogi et al., 2001). Although nearly all mycobacteria are saprophytes or non-pathogenic to humans, a few species cause diseases resulting in pulmonary and extra-pulmonary infections that can affect nearly all organs. Infections, which are caused by strict or opportunistic pathogenic mycobacteria (***Figure 1***) pose a sustained threat to human health. Of these, tuberculosis (TB), caused by *Mycobacterium tuberculosis* (*Mtb*), is the most serious,

leading to ~ 1.2 million fatalities per year (World Health Organization, 2019). Infections involving other pathogenic mycobacteria, e.g. *M. abscessus* and *M. avium complex*, are on the rise with some outnumbering those caused by *M. tuberculosis* in countries including the United States (Donohue, 2018; Johansen et al., 2020). These infections are notoriously difficult to treat due to intrinsic or emerging resistance to many common antibiotics, thus exacerbating the challenge to find suitable drug targets.

Oxidative phosphorylation (OXPHOS) has gained interest as a target space for antibiotic drug development (Cook et al., 2017; Hards et al., 2020). In OXPHOS, the protein complexes of the electron transport chain (ETC) establish a proton motive force (PMF) across a biomembrane that drives the synthesis of adenosine triphosphate (ATP) by ATP synthase (Mitchell, 1961). Maintenance of PMF and ATP homeostasis is required for the survival of both replicative and non-replicative (often referred to as dormant) mycobacteria and its dissipation leads to a rapid loss of cell viability and cell death (Koul et al., 2008; Rao et al., 2008). The reliance on the PMF and ATP homeostasis thus highlights the importance of the mycobacterial proton-pumping cytochrome *bcc-aa*$_3$ supercomplex, which consists of a *bcc* menaquinol reductase (complex III, CIII) and an *aa*$_3$ oxidase (complex IV, CIV) that are tightly associated (Gong et al., 2018; Kim et al., 2015; Megehee et al., 2006). Several studies support the attractiveness of cytochrome *bcc-aa*$_3$ for mycobacterial drug development (de Jager et al., 2020; Liu et al., 2019; Lu et al., 2018; Pethe et al., 2013; Scherr et al., 2018). Given the strict sequence conservation of this complex (***Figure 1***), broad spectrum activity of a therapeutic within the pathogenic mycobacteria is likely (Lee et al., 2020). Interestingly, all the cytochrome *bcc-aa*$_3$ inhibitors published to date appear to target the QcrB subunit (***Figure 1***) of the cytochrome *bcc* complex and are likely bound to the menaquinol binding (Qp) site of the QcrB subunit (Lee et al., 2020). The most advanced of these are Q203 and TB47, which have been shown to clear infections due to *M. tuberculosis* (de Jager et al., 2020; Lu et al., 2018; Pethe et al., 2013) and *M. ulcerans* (Liu et al., 2019; Scherr et al., 2018). Q203 has recently completed phase II clinical

trials for TB treatment (ClinicalTrials.gov number, NCT03563599) (de Jager et al., 2020). TB47 has also been evaluated in a preclinical study (http://www.newtbdrugs.org/pipeline/discovery).

To progress an understanding of the cytochrome *bcc* structure and its interaction with new drug leads, here we have determined the atomic resolution cryo-electron microscopy (cryo-EM) structures of *M. tuberculosis* cytochrome *bcc* alone (2.68 Å resolution) and in complex with Q203 (2.67 Å resolution) and TB47 (2.93 Å resolution). The high resolution *M. tuberculosis* cytochrome *bcc* structures will greatly accelerate efforts towards structure-guided drug discovery for pathogenic mycobacteria including *M. tuberculosis*.

Results and Discussion

Structure of *M. tuberculosis* cytochrome *bcc*

A hybrid supercomplex consisting of *M. tuberculosis* CIII and *Mycobacterium smegmatis* CIV was purified and its structure determined by cryo-EM to an overall resolution of 2.68 Å (***Figure 2-figure supplement 1; Supplementary file 1***). The *M. tuberculosis* cytochrome *bcc* is dimeric similar to the *M. smegmatis bcc* complex in the CIII/CIV supercomplex (Gong et al., 2018) and the bovine mitochondrial cytochrome bc_1 complex (Iwata et al., 1998) (***Figure 2A, B***). The dimensions of the complex are 140 Å by 70 Å by 100 Å (***Figure 2A, B***). Three canonical subunits QcrA, QcrB and QcrC with all the prosthetic groups and endogenous menaquinones were clearly assigned in the unambiguous cryo-EM density (***Figure 2C; Figure 2-figure supplement 2***). QcrA has three transmembrane helices (TMHs) and has a "U" shaped structure (***Figures 2D, 3A***). The N-terminal region with TMH1/2 and the TMH3 make up the two arms of the "U" structure. These arms are linked by the region located near the cytoplasmic side. Attached to $_{QcrA}$TMH3 is the C-terminal domain, which faces the periplasmic side of the membrane and holds the [2Fe-2S] cluster in place. QcrB has eight TMHs (***Figures 2D, 3B***). Four of these are responsible for burying two functionally important heme *b* cofactors (high potential heme b_H and low potential heme b_L). Both heme b_L and

heme b_H are bound between TMH I/II and TMH III/IV, heme b_L is near the periplasmic side and heme b_H near the cytoplasmic side. QcrC is a transmembrane protein with a C-terminal TMH located between $_{QcrB}$TMH5 and $_{QcrB}$TMH7 (***Figures 2D, 3C***). The N-terminal periplasmic portion of QcrC can be divided into two heme-containing cytochrome *c* domains designated D1 and D2. The D1 domain protrudes out of the core of CIII whereas the D2 domain interacts extensively with QcrA and QcrB.

Quinone and quinone binding pockets of *M. tuberculosis* cytochrome *bcc*

Quinone binding sites are often species-dependent and thus are important for drug discovery (Harikishore et al., 2020; Lee et al., 2020). Two quinone-binding sites could be identified (***Figure 3D, E***), the quinol oxidation site (Q_P site) and the quinone reduction site (Q_N site). The Q_P site responsible for menaquinol (MKH_2) oxidation is near heme b_L, whereas the Q_N site responsible for menaquinone (MK) reduction is close to heme b_H (***Figure 3D, E; Figure 2-figure supplement 2***). The Q_P site is at the center of an inverted triangle structure surrounded by helices (***Figure 3D***). One MK molecule was identified at this site with its naphthoquinone ring surrounded mainly by hydrophobic residues, $_{QcrB}$Phe158, $_{QcrB}$Tyr161, $_{QcrB}$Leu180, $_{QcrB}$Ile183, $_{QcrB}$Met310 and $_{QcrB}$Met342. Its hydrophobic tail that contains multiple isoprenoid groups wraps around $_{QcrB}$TMH6 down to its cytoplasmic end by interacting with $_{QcrB}$Met187, $_{QcrB}$Ala339, $_{QcrB}$Leu344 and $_{QcrB}$Val347. However, the edge-to-edge distance from MK to heme b_L is 15 Å. Thus, we speculate that the endogenous electron donor MKH_2 should be closer to the heme b_L to facilitate electron transfer. We speculate that what is observed here is the oxidized product as it leaves the Q_P site. It is worth noting that all the reported inhibitors including Q203 (Pethe et al., 2013) and TB47 (Lu et al., 2018) are suggested to interact with this Q_P site. In addition, the Q_N site is mainly formed by $_{QcrB}$TMH1, $_{QcrB}$TMH4, $_{QcrB}$TMH5 and one loop region of QcrB (***Figure 3E***). The head group of MK is bound in this pocket interacting with $_{QcrB}$Phe39, $_{QcrB}$Glu49, $_{QcrB}$Leu225, $_{QcrB}$Leu232, $_{QcrB}$Trp236 and $_{QcrB}$Phe262, and its long hydrophobic tail extends along $_{QcrB}$TMH1 towards the periplasmic side. MK/MKH_2 are part of

the Q-cycle hypothesis and essential for electron transfer in the cytochrome *bcc* complex (Gong et al., 2018). In addition, the electron transfer pathway of *M. tuberculosis* cytochrome *bcc* is believed to be same as that of *M. smegmatis* cytochrome *bcc* based on their highly similar cofactor arrangement (Gong et al., 2018). Given the crossspecies activity of this complex (Lee et al., 2020) and high homology of the QcrB subunits across mycobacterial pathogens (***Figure 1***), this data opens the way for the discovery of broad spectrum mycobacterial agents based on rational, structure-based inhibitor design principles.

Q203 interactions in *M. tuberculosis* cytochrome *bcc* binding pocket

Q203 has recently been subjected to a phase II clinical study for *M. tuberculosis* treatment (de Jager et al., 2020). This compound has also been shown to be strongly bactericidal against *Mycobacterium ulcerans* (Scherr et al., 2018). It is suggested to be an inhibitor that competes with endogenous substrate binding (Q_P site) of the cytochrome *bcc* complex (Pethe et al., 2013), but this hypothesis is yet to be verified by direct experimental evidence. To obtain atomic information on the mode of binding of Q203 to cytochrome *bcc*, we have determined the structure of a hybrid supercomplex as described above in the presence of Q203 by cryo-EM to an overall resolution of 2.67 Å (***Figure 4-figure supplement 1 and figure supplement 2; Supplementary file 1***). The cryo-EM map shows that close to the Qp binding pocket within the membrane of each QcrB of cytochrome *bcc*, density for Q203 is present (***Figure 4A, B***). All of the Q203 molecules fill each QcrB subunit binding deeply into the Q_P pocket and with identical binding modes. The key interactions that anchor Q203 are (i) a hydrogen bond between the hydroxyl oxygen of the side chain of $_{QcrB}$Thr313 and the amine in the carboxamide linker of Q203 (3.0 Å), (ii) a halogen bond between the chlorine atom of the trifluoromethyl group and an ordered water molecule that simultaneously forms a hydrogen bond with the hydroxyl oxygen of the side chain of $_{QcrB}$Tyr164, (iii) a hydrogen bond between the side chain of $_{QcrB}$Glu314 and the nitrogen atom in the imidazopyridine ring (3.0 Å), and (iv) a hydrogen bond between the side chain of $_{QcrA}$His375 and the nitrogen atom in the imidazopyridine ring (2.98 Å)

(***Figure 4C***). In addition, the carbon atoms of Q203 interacts with Gly^{175}, Ala^{179}, Leu^{180}, Thr^{184}, Ser^{304}, Pro^{306}, Met^{310}, Ala^{317} and Met^{342} through hydrophobic interactions. These residues are within helices adjacent to QcrB. Consistent with these findings, functional studies have shown that substitution of $_{QcrB}$Thr313 to alanine confers resistance to the Q203 (Pethe et al., 2013). Interestingly, the binding of Q203 involves residues from both QcrA and QcrB. Due to the need to form stabilizing interactions between subunits, resistance may be more difficult to achieve here than if the site involved only one subunit. Furthermore, the mapping of reported mutations in Q203-resistant *M. tuberculosis* reveals that they are positioned directly where Q203 binds in this structure (Lupien et al., 2020) (***Figure 4-figure supplement 3***).

TB47 binding mode of *M. tuberculosis* cytochrome *bcc*

TB47, currently being evaluated in preclinical studies, has also been reported to target the QcrB of cytochromes *bcc* from *M. tuberculosis* (Lu et al., 2018) and *M. ulcerans* (Liu et al., 2019). Here we have determined its structure in complex with the hybrid mycobacterial cytochrome *bcc*. The 2.93 Å cryo-EM map shows density for TB47 and confirms that it binds in the same location as Q203 (***Figure 5A, B; Figure 5-figure supplement 1 and figure supplement 2; Supplementary file 1***). Three hydrogen bond interactions are observed involving the side chains of $_{QcrB}$Thr313, $_{QcrB}$Glu314, and $_{QcrA}$His375. Similar interactions are also observed when Q203 binds (***Figure 5C***). Tyr^{161}, Leu^{171}, Gly^{175}, Ala^{179}, Leu^{180}, Thr^{184}, Met^{187}, Leu^{194}, Ser^{304}, Gly^{305} and Met^{342} also contribute to TB47 binding, largely through hydrophobic interactions (***Figure 5C***). A mutation in TB47-resistant *M. smegmatis* (*M. tuberculosis*: H195Y) is positioned close to the Qp-binding site (Lu et al., 2018) (***Figure 5-figure supplement 3***). As a result, it causes indirect steric interference with the binding of TB47, thus this structure provides the molecular basis for conferring resistance.

Specificity of Q203 and TB47 for mycobacterial cytochromes *bcc* complex

The basis for the high specificity of Q203 and TB47 toward the Qp site of mycobacterial cytochromes *bcc* becomes apparent in the structural comparison between the QcrB subunit of *M.*

tuberculosis and counterparts from other species (***Figure 6***). The highly conserved residues that are involved in the binding of these two molecules in this region (***Figure 6-figure supplement 1***) suggest a consistent overall fold and binding site exists in mycobacteria. This is also in agreement with the fact that Q203 and TB47 show antimycobacterial activity across many species (de Jager et al., 2020; Liu et al., 2019; Lu et al., 2018; Pethe et al., 2013; Scherr et al., 2018). In contrast, in other prokaryotic, eukaryotic and human Qp-binding pockets, for example, from *Saccharomyces cerevisiae* (Lange and Hunte, 2002), *Rhodobacter sphaeroides* (Esser et al., 2008) or human (Guo et al., 2017), many of the observed interactions would be sterically hindered (***Figure 6***). This suggests that Q203 and TB47 should have low binding affinity toward its counterpart QcrB in non-mycobacterial bacteria and in eukaryotes. Coincidentally, the residues contributing to the clashes of Q203 and TB47 in the Qp binding pockets are commonly observed (***Figure 6***). Even if there is some flexibility in the Qp binding pocket that enables some level of binding, key residues that enable the binding of Q203 and TB47 in the mycobacteria are not present in other bacteria and eukaryotes (***Figure 6-figure supplement 1***). These observations correlate with low general antibacterial activity and low cytotoxicity for Q203 and TB47 (Liu et al., 2019; Lu et al., 2018; Pethe et al., 2013; Scherr et al., 2018).

Implication of Q203 and TB47 inhibitory mechanism

To gain further insights into the mechanism of action of Q203, we compared the structures of *M. tuberculosis* cytochrome *bcc* in the presence and absence of Q203 (***Figure 7-figure supplement 1A***). The structure of apo cytochrome *bcc* is almost identical with the Q203-bound structure (rmsd of 0.497 Å for all Ca atoms), which suggests that Q203 binding does not significantly affect the overall architecture of cytochrome *bcc*. A comparison of the Q203-bound and Q203-free cytochrome *bcc* structures shows residues involved in the binding pocket move outward, thus adapting to the shape of Q203 (***Figure 7-figure supplement 1B***). Specifically, the side chains of $_{QcrB}$Ser304, $_{QcrB}$Glu313, $_{QcrB}$Glu314 and $_{QcrB}$Met342 undergo significant conformational changes to form

hydrogen bonds to Q203. The binding of TB47 to *M. tuberculosis* cytochrome *bcc* also induces very similar conformational changes in the Qp binding pocket to those seen for Q203 (rmsd of 0.454 Å for all Ca atoms) (***Figure 7-figure supplement 1B***). Differences in binding are due to the different ethyl group and methyl moieties in the head groups of Q203 and TB47, respectively. It is also important to note that one endogenous substrate molecule is also bound to the Qp site in the apo structure of cytochrome *bcc*, which potentially affects the evaluation of the conformational changes upon the binding of Q203 or TB47.

When analyzing the superimposed structures (***Figure 7-figure supplement 1***), it is apparent that Q203 and TB47 act competitively with the quinol binding as they almost completely occupy the Qp pocket. We therefore conclude that Q203 and TB47 are bona fide analogs of the substrate, and thus ultimately function by hindering the downstream synthesis of ATP (***Figure 7A***). These two compounds are also highly bactericidal against *M. ulcerans*, almost certainly targeting the Qp-binding site (Liu et al., 2019; Scherr et al., 2018). In summary, the sequences of the QcrB subunits have high homology across pathogenic mycobacteria (Lee et al., 2020) and the essential residues ($_{QcrB}$Glu313 and $_{QcrB}$Glu314) that are involved in hydrogen-bonding interactions with the inhibitors (Pethe et al., 2013; Scherr et al., 2018) are conserved across pathogenic mycobacteria (***Figure 7B***) .

Conclusions

We have determined the apo- and Q203 and Tb47-bound structures of a hybrid pathogenic *M. tuberculosis/M. smegmatis* cytochrome *bcc* complex. The study shows the structural features of *M. tuberculosis* cytochrome *bcc* of and how it is specifically inhibited by Q203 and TB47. The extensive interactions between Q203 or TB47 and the Qp binding pocket account for the highly specific binding of these two inhibitors to pathogenic *M. tuberculosis* cytochromes *bcc* compared to eukaryotic counterparts. Two conservative residues involved with the formation of hydrogen bonds are observed across the pathogenic mycobacteria. These structures provide a long-sought basis for

225 rational, structure-based inhibitor design to accelerate the development of Q203 and TB47 analogs as
226 drug leads for mycobacterial infections.

227

228 **Materials and Methods**

229 **Key resources table**

REAGENT or RESOURCE	SOURCE	IDENTIFIER
Bacterial and Virus Strains		
M. smegmatis MC^2 51	(Li et al., 2014)	
Chemicals, Peptides, and Recombinant Proteins		
Lauryl Maltose Neopentyl Glycol (LMNG)	Anatrace	Cat# NG310
Digitonin	BIOSYNTH	Cat# D-3200
Critical Commercial Assays		
Ni-NTA Agarose	QIAGEN	Cat# 30230
Superdex 200 increase	GE Healthcare	Cat# 28990944
Deposited Data		
EM map apo complex	This paper	EMDB code: EMD-30943
Apo complex structure	This paper	PDB code: 7E1V
EM map Q203-bound complex	This paper	EMDB code: EMD-30944
Q203-bound complex structure	This paper	PDB code: 7E1W
EM map TB47-bound complex	This paper	EMDB code: EMD-30945
TB47-bound complex structure	This paper	PDB code: 7E1X
Software and Algorithms		
SerialEM	(Mastronarde, 2003)	http://bio3d.colorado.edu/SerialEM/
MotionCor2	(Zheng et al., 2017)	https://emcore.ucsf.edu/ucsf-motioncor2
RELION	(Zivanov et al., 2019)	https://www2.mrc-lmb.cam.ac.uk/relion
cryoSPARC	(Punjani et al., 2017)	https://cryosparc.com/
Phyre2	(Kelley et al., 2015)	http://www.sbg.bio.ic.ac.uk/phyre2/html/page.cgi?id=index
UCSF Chimera	(Pettersen et al., 2004)	https://www.cgl.ucsf.edu/chimera/
COOT	(Emsley et al., 2010)	https://www2.mrc-lmb.cam.ac.uk/personal/pemsley/coot/
PHENIX	(Adams et al., 2010)	https://www.phenix-

PyMOL	(Schrodinger, 2010)	online.org/ https://pymol.org/2/
Other		
100kDa cutoff concentrators	Sartorius	Cat# VS0642
R0.6/1.0 300 mesh Cu holey carbon grids	Quantifoil	

230

231 **Expression of hybrid supercomplex consisting of *Mtb* CIII and *Msm* CIV**

232 The hybrid supercomplex was obtained according to a previous study (Kim et al., 2015) but with
233 some modifications. The *Mtb* cytochrome *bcc* complex is encoded by three putative genes (Rv2194-
234 2196). Genes were amplified from H37Rv genomic DNA by PCR using Phanta Max DNA
235 polymerase (Vazyme), and two steps PCR was used to inset a 10 × His tag at the C-terminus of the
236 qcrB (Rv2196). Genes encoding the entire cytochrome *bcc* complex operon were then cloned into
237 the vector pVV16. The resultant plasmid was transformed into *M. smegmatis* mc^2 51 (Li et al., 2014)
238 cells whose qcrCAB operon encoding *Msm* cytochrome *bcc* had already been knocked out. The cells
239 were cultivated in Luria-Bertain broth (LB) liquid media supplemented with 50 μg/mL hygromycin,
240 25 μg/mL streptomycin and 0.1% Tween 80. Cell pellets were harvested by centrifugation when the
241 cells were grown to an optical density (OD_{600} of 1.0-1.2) at 37 °C (220rpm). Harvested cells were
242 frozen at -80 °C until use.

243 **Purification of the hybrid supercomplex**

244 Cell pellets were thawed and resuspended in buffer A containing 20 mM MOPS, pH 7.4, 100 mM
245 NaCl, and then lysed by passing through a French Press at 1,200bar three times. Cell debris and non-
246 lysed cells were removed by centrifugation at 14,000 rpm for 10 min at 4 ºC. The supernatant was
247 collected and ultra-centrifuged at 36,900 rpm and 4 ºC for 2 h. The membrane fraction was
248 solubilized by addition of 1% (w/v) LMNG (lauryl maltose neopentyl glycol) in buffer A and
249 incubated for 2 h at 4 ºC with slow stirring. The suspension was ultra-centrifuged and the supernatant
250 was applied to Ni-NTA agarose beads (GE Healthcare) at 4 ºC. The beads were further washed in
251 buffer A with 50 mM imidazole and 0.004% (w/v) LMNG. The buffer was exchanged to buffer B

(20 mM MOPS, pH 7.4, 100 mM NaCl and 0.1% (w/v) digitonin) and then washed in resin in batch mode. The protein was eluted from the beads with buffer B containing 500 mM imidazole. Protein was then concentrated and loaded onto a Superdex 6 increase (10/300 GL, GE Healthcare) column equilibrated in buffer B. Peak fractions were pooled and concentrated to ~ 8 mg/ml for electron microscopy studies.

Cryo sample preparation and data collection

300-mesh Quantifoil R0.6/1.0 grids (Quantifoil, Micro Tools GmbH, Germany) were glow-discharged at H_2/O_2 atmosphere for 25s. 3 μL aliquots of protein complex at a concentration of 10 mg/mL were applied to the grid and then blotted for 3s with force 0 at 8°C and 100% humidity using a Vitrobot IV (Thermo). Images were collected using a Titan Krios 300keV electron microscope (Thermo), equipped with K3 Summit direct electron detector camera (Gatan). Data was recorded at 29,000× magnification with a calibrated super-resolution pixel size 0.82 Å/pixel. The exposure time was set to 2.4 s with 40 subframes and a total dose of 60 electrons per $Å^2$. All images were automatically recorded using SerialEM with a defocus range from 1.2 μm to 1.8 μm (Mastronarde, 2003). For the datasets of apo, Q203-bound and TB47-bound *M. tuberculosis* cytochrome *bcc*, a total of 4,141, 3,763 and 2,968 images were collected, respectively.

Image processing

All dose-fractioned stacks were motion-corrected and dose-weighted using MotionCorr2 (Zheng et al., 2017) in RELION (Zivanov et al., 2019). CTF estimation was conducted using cryoSPARC patch CTF estimation (Punjani et al., 2017). For the dataset of apo hybrid *M. tuberculosis* cytochrome *bcc*, 1,208,054 particles were picked automatically using EMD-9610 map as the template and extracted with a box size of rescaled 256 pixels (binned 2). 327,188 particles were selected after two rounds of 2D classification. 100,000 particles were used to perform Ab-Initio reconstruction in four classes, and these four classes were used as 3D volume templates for heterogeneous refinement with all selected particles. 112,804 particles converged into one class with

277 clear signals and then re-extracted with 512 pixels. Next, this particle set was used to do
278 homogeneous refinement and local refinement, yielding the final resolution 2.68 Å. For the dataset
279 of Q203-bound and TB47-bound *M. tuberculosis* cytochrome *bcc*, the data processing was
280 performed in a similar pipeline, resulting in the final reconstruction resolution at 2.67 Å and 2.93 Å,
281 respectively (detailed parameters shown in supplementary figures).

282 **Model building and validation**

283 The *M. smegmatis* respiratory complex $CIII_2CIV_2$ (PDB code: 6ADQ) model (Gong et al., 2018) as
284 rigid body was fitted into EM density maps using UCSF Chimera 1.12 (Pettersen et al., 2004). Next,
285 the resultant atomic model was manually modified according to the subunit sequences of *M.*
286 *tuberculosis* cytochrome *bcc* and refined in COOT 0.8.9.1 (Emsley et al., 2010), followed by real-
287 space refinement in PHENIX (Adams et al., 2010). The smile strings of Q203 and TB47 were
288 generated and copied from ChemDraw (Li et al., 2004) and defined in PHENIX elBOW. Q203 and
289 TB47 were manually built into the corresponding EM densities. The local resolution map was
290 calculated in cryoSPARC (Punjani et al., 2017). All reported resolutions were based on the gold-
291 standard FSC 0.143 criteria (Rosenthal and Henderson, 2003).

292 **Creation of Figures**

293 All the figures were created using UCSF Chimera (Pettersen et al., 2004) or PyMOL (Schrodinger,
294 2010).

295 **Data availability:**

296 The accession numbers for the 3D cryo-EM density map of apo, Q203-bound and TB47-bound
297 hybrid supercomplex in present study are EMD-30943, EMD-30944 and EMD-30945, respectively.
298 The accession numbers for the coordinates for the apo, Q203-bound and TB47-bound hybrid
299 supercomplex in this study are PDB: 7E1V, PDB: 7E1W and PDB: 7E1X, respectively.
300 Correspondence and requests for materials should be addressed to the corresponding authors. The
301 following datasets were generated:

Author(s)	Year	Dataset title	Dataset URL	Database and Identifier
Zhou, S., Wang, W., Gao, Y., Gong, H., Rao, Z.	2021	Cryo-EM structure of apo hybrid respiratory supercomplex consisting of Mycobacterium tuberculosis complexIII and Mycobacterium smegmatis complexIV	https://www.ebi.ac.uk/pdbe/entry/emdb/EMD-30943	Electron Microscopy Data Bank, EMD-30943
Zhou, S., Wang, W., Gao, Y., Gong, H., Rao, Z.	2021	Cryo-EM structure of apo hybrid respiratory supercomplex consisting of Mycobacterium tuberculosis complexIII and Mycobacterium smegmatis complexIV	https://www.rcsb.org/structure/7E1V	Protein Data Bank, 7E1V
Zhou, S., Wang, W., Gao, Y., Gong, H., Rao, Z.	2021	Cryo-EM structure of hybrid respiratory supercomplex consisting of Mycobacterium tuberculosis complexIII and Mycobacterium smegmatis complexIV in the presence of Q203	https://www.ebi.ac.uk/pdbe/entry/emdb/EMD-30944	Electron Microscopy Data Bank, EMD-30944
Zhou, S., Wang, W., Gao, Y., Gong, H., Rao, Z.	2021	Cryo-EM structure of hybrid respiratory supercomplex consisting of Mycobacterium tuberculosis complexIII and Mycobacterium smegmatis complexIV in the presence of Q203	https://www.rcsb.org/structure/7E1W	Protein Data Bank, 7E1W
Zhou, S., Wang, W., Gao, Y., Gong, H., Rao, Z.	2021	Cryo-EM structure of hybrid respiratory supercomplex consisting of Mycobacterium tuberculosis complexIII and Mycobacterium smegmatis complexIV in presence of TB47	https://www.ebi.ac.uk/pdbe/entry/emdb/EMD-30945	Electron Microscopy Data Bank, EMD-30945
Zhou, S., Wang, W., Gao, Y., Gong, H., Rao, Z.	2021	Cryo-EM structure of hybrid respiratory supercomplex consisting of Mycobacterium tuberculosis complexIII and Mycobacterium smegmatis complexIV in presence of TB47	https://www.rcsb.org/structure/7E1X	Protein Data Bank, 7E1X

Acknowledgments

We thank Dr. Chao Peng of the Mass Spectrometry System at the National Facility for Protein Science in Shanghai (NFPS), Zhangjiang Lab, SARI, China for data collection and analysis and Prof. Kaixia Mi (CAS Key Laboratory of Pathogenic Microbiology and Immunology, Institute of Microbiology, CAS) for sharing the strain *M. smegmatis* mc^2 51. We would like to thank Prof. Gregory M. Cook (School of Biomedical Sciences, University of Otago, New Zealand) and Prof. Xiaoyun Lu (School of Pharmacy, Ji′nan University, China) for kindly providing TB47 for this study. We would also like to thank the Bio-Electron Microscopy Facility of ShanghaiTech University.

Additional information

Funding

Funder	Grant reference number	Author
National Key Research and Development Program of China	2017YFC0840300	Zihe Rao
National Key Research and Development Program of China	2020YFA0707500	Zihe Rao
National Natural Science Foundation of China	81520108019	Zihe Rao
National Natural Science Foundation of China	813300237	Zihe Rao
Tianjin Natural Science Foundation	20JCQNJC01430	Hongri Gong

Author contributions

Shan Zhou, Data curation, Formal analysis, Methodology, Writing—original draft, Writing—review and editing; Weiwei Wang, Data curation, Formal analysis, Methodology, Visualization, Writing—review and editing; Xiaoting Zhou, Yuying Zhang, Yuezheng Lai, Yanting Tang, Jinxu Xu, Xiaolin Yang, Quan Wang, Formal analysis, Methodology; Luke W. Guddat, Formal analysis, Writing—review and editing; Yan Gao, Data curation, Formal analysis, Methodology, Visualization, Writing—review and editing; Zihe Rao, Resources, Supervision, Funding acquisition, Writing—

review and editing; Hongri Gong, Conceptualization, Investigation, Funding acquisition, Formal analysis, Methodology, Writing—original draft, Writing—review and editing.

Competing interests

The authors declare no competing interests.

References

Adams PD, Afonine PV, Bunkoczi G, Chen VB, Davis IW, Echols N, Headd JJ, Hung LW, Kapral GJ, Grosse-Kunstleve RW, McCoy AJ, Moriarty NW, Oeffner R, Read RJ, Richardson DC, Richardson JS, Terwilliger TC, Zwart PH. 2010. PHENIX: a comprehensive Python-based system for macromolecular structure solution. *Acta Crystallographica. Section D: Biological Crystallography* **66**: 213-221. doi: 10.1107/S0907444909052925.

Chisholm RH, Trauer JM, Curnoe D, Tanaka MM. 2016. Controlled fire use in early humans might have triggered the evolutionary emergence of tuberculosis. *Proceedings of the National Academy of Sciences of the United States of America* **113**: 9051-9056. doi: 10.1073/pnas.1603224113.

Cole ST, Eiglmeier K, Parkhill J, James KD, Thomson NR, Wheeler PR, Honore N, Garnier T, Churcher C, Harris D, Mungall K, Basham D, Brown D, Chillingworth T, Connor R, Davies RM, Devlin K, Duthoy S, Feltwell T, Fraser A, Hamlin N, Holroyd S, Hornsby T, Jagels K, Lacroix C, Maclean J, Moule S, Murphy L, Oliver K, Quail MA, Rajandream MA, Rutherford KM, Rutter S, Seeger K, Simon S, Simmonds M, Skelton J, Squares R, Squares S, Stevens K, Taylor K, Whitehead S, Woodward JR, Barrell BG. 2001. Massive gene decay in the *leprosy bacillus*. *Nature* **409**: 1007-1011. doi: 10.1038/35059006.

Cook GM, Hards K, Dunn E, Heikal A, Nakatani Y, Greening C, Crick DC, Fontes FL, Pethe K, Hasenoehrl E, Berney M. 2017. Oxidative phosphorylation as a target space for tuberculosis: success, caution, and future directions. *Microbiology spectrum* **5**: 295-316. doi: 10.1128/microbiolspec.TBTB2-0014-2016.

348 de Jager VR, Dawson R, van Niekerk C, Hutchings J, Kim J, Vanker N, van der Merwe L, Choi J,
349 Nam K, Diacon AH. 2020. Telacebec (Q203), a new antituberculosis agent. *New England Journal of*
350 *Medicine* **382**: 1280-1281. doi: 10.1056/NEJMc1913327.
351 Donohue MJ. 2018. Increasing nontuberculous mycobacteria reporting rates and species diversity
352 identified in clinical laboratory reports. *BMC Infectious Diseases* **18**: 163. doi: 10.1186/s12879-018-
353 3043-7.
354 Emsley P, Lohkamp B, Scott WG, Cowtan K. 2010. Features and development of Coot. *Acta*
355 *Crystallogr D Biol Crystallogr* **66**: 486-501. doi: 10.1107/s0907444910007493.
356 Esser L, Elberry M, Zhou F, Yu CA, Yu L, Xia D. 2008. Inhibitor-complexed structures of the
357 cytochrome bc_1 from the photosynthetic bacterium *Rhodobacter sphaeroides*. *Journal of Biological*
358 *Chemistry* **283**: 2846-2857. doi: 10.1074/jbc.M708608200.
359 Gong H, Li J, Xu A, Tang Y, Ji W, Gao R, Wang S, Yu L, Tian C, Li J, Yen HY, Man Lam S, Shui G,
360 Yang X, Sun Y, Li X, Jia M, Yang C, Jiang B, Lou Z, Robinson CV, Wong LL, Guddat LW, Sun F,
361 Wang Q, Rao Z. 2018. An electron transfer path connects subunits of a mycobacterial respiratory
362 supercomplex. *Science* **362**: eaat8923. doi: 10.1126/science.aat8923.
363 Guo R, Zong S, Wu M, Gu J, Yang M. 2017. Architecture of human mitochondrial respiratory
364 megacomplex $I_2III_2IV_2$. *Cell* **170**: 1247-1257. e1212. doi: 10.1016/j.cell.2017.07.050
365 Hards K, Adolph C, Harold LK, McNeil MB, Cheung CY, Jinich A, Rhee KY, Cook GM. 2020. Two
366 for the price of one: Attacking the energetic-metabolic hub of mycobacteria to produce new
367 chemotherapeutic agents. *Progress in Biophysics and Molecular Biology* **152**: 35-44. doi:
368 10.1016/j.pbiomolbio.2019.11.003.
369 Harikishore A, Chong SSM, Ragunathan P, Bates RW, Grüber G. 2021. Targeting the menaquinol
370 binding loop of mycobacterial cytochrome *bd* oxidase. *Molecular diversity* **25**: 517-524. doi:
371 10.1007/s11030-020-10034-0
372 Iwata S, Lee JW, Okada K, Lee JK, Iwata M, Rasmussen B, Link TA, Ramaswamy S, Jap BK. 1998.

373 Complete structure of the 11-subunit bovine mitochondrial cytochrome *bc$_1$* complex. *Science* **281**:
374 64-71. doi: 10.1126/science.281.5373.64
375 Johansen MD, Herrmann JL, Kremer L. 2020. Non-tuberculous mycobacteria and the rise of
376 *Mycobacterium abscessus*. *Nature Reviews: Microbiology* **18**: 392-407. doi: 10.1038/s41579-020-
377 0331-1.
378 Kelley LA, Mezulis S, Yates CM, Wass MN, Sternberg MJ. 2015. The Phyre2 web portal for protein
379 modeling, prediction and analysis. *Nature Protocols* **10**: 845–858. doi: 10.1038/nprot.2015.053.
380 Kim M-S, Jang J, Rahman NBA, Pethe K, Berry EA, Huang L-S. 2015. Isolation and
381 characterization of a hybrid respiratory supercomplex consisting of *Mycobacterium tuberculosis*
382 cytochrome *bcc* and *Mycobacterium smegmatis* cytochrome *aa$_3$*. *The Journal of biological chemistry*
383 **290**: 14350-14360. doi: 10.1074/jbc.M114.624312
384 Koul A, Vranckx L, Dendouga N, Balemans W, Van den Wyngaert I, Vergauwen K, Gohlmann HWH,
385 Willebrords R, Poncelet A, Guillemont J, Bald D, Andries K. 2008. Diarylquinolines are bactericidal
386 for dormant mycobacteria as a result of disturbed ATP homeostasis. *Journal of Biological Chemistry*
387 **283**: 25273-25280. doi: 10.1074/jbc.M803899200.
388 Lange C, Hunte C. 2002. Crystal structure of the yeast cytochrome *bc$_1$* complex with its bound
389 substrate cytochrome *c*. *Proceedings of the National Academy of Sciences of the United States of*
390 *America* **99**: 2800-2805. doi: 10.1073/pnas.052704699.
391 Lee BS, Sviriaeva E, Pethe K. 2020. Targeting the cytochrome oxidases for drug development in
392 mycobacteria. *Progress in biophysics and molecular biology* **152**: 45-54. doi:
393 10.1016/j.pbiomolbio.2020.02.001
394 Li X, Liu F, Hu Y, Mi K. 2014. Draft Genome Sequence of mc^{2}51, a Highly Hydrogen Peroxide-
395 Resistant *Mycobacterium smegmatis* Mutant Strain. *Genome announcements* **2**: doi:
396 10.1128/genomeA.00092-14.
397 Li Z, Wan H, Shi Y, Ouyang P. 2004. Personal experience with four kinds of chemical structure

398 drawing software: review on ChemDraw, ChemWindow, ISIS/Draw, and ChemSketch. *Journal of*
399 *chemical information and computer science* **44**: 1886-1890. doi: 10.1021/ci049794h.
400 Liu Y, Gao Y, Liu J, Tan Y, Liu Z, Chhotaray C, Jiang H, Lu Z, Chiwala G, Wang S. 2019. The
401 compound TB47 is highly bactericidal against *Mycobacterium ulcerans* in a Buruli ulcer mouse
402 model. *Nature communications* **10**: 1-9. doi: 10.1371/journal.ppat.1008270.
403 Lu X, Williams Z, Hards K, Tang J, Cheung C-Y, Aung HL, Wang B, Liu Z, Hu X, Lenaerts A. 2018.
404 Pyrazolo [1, 5-a] pyridine inhibitor of the respiratory cytochrome *bcc* complex for the treatment of
405 drug-resistant tuberculosis. *ACS infectious diseases* **5**: 239-249. doi: 10.1021/acsinfecdis.8b00225
406 Lupien A, Foo CS-Y, Savina S, Vocat A, Piton J, Monakhova N, Benjak A, Lamprecht DA, Steyn AJ,
407 Pethe K, Makarov VA, Cole ST. 2020. New 2-Ethylthio-4-methylaminoquinazoline derivatives
408 inhibiting two subunits of cytochrome bc_1 in *Mycobacterium tuberculosis*. *PLoS pathogens* **16**:
409 e1008270. doi: 10.1371/journal.ppat.1008270
410 Mastronarde DN. 2003. SerialEM: a program for automated tilt series acquisition on Tecnai
411 microscopes using prediction of specimen position. *Microscopy and Microanalysis* **9**: 1182-1183. doi:
412 10.1017/S1431927603445911
413 Megehee JA, Hosler JP, Lundrigan MD. 2006. Evidence for a cytochrome *bcc–aa*$_3$ interaction in the
414 respiratory chain of *Mycobacterium smegmatis*. *Microbiogy (Reading England)* **152**: 823-829. doi:
415 10.1099/mic.0.28723-0.
416 Mitchell P. 1961. Coupling of phosphorylation to electron and hydrogen transfer by a chemi-osmotic
417 type of mechanism. *Nature* **191**: 144-148. doi: 10.1038/191144a0
418 World Health Organization. 2019. Global Tuberculosis Report.
419 Pethe K, Bifani P, Jang J, Kang S, Park S, Ahn S, Jiricek J, Jung J, Jeon HK, Cechetto J, Christophe
420 T, Lee H, Kempf M, Jackson M, Lenaerts AJ, Pham H, Jones V, Seo MJ, Kim YM, Seo M, Seo JJ,
421 Park D, Ko Y, Choi I, Kim R, Kim SY, Lim S, Yim SA, Nam J, Kang H, Kwon H, Oh CT, Cho Y,
422 Jang Y, Kim J, Chua A, Tan BH, Nanjundappa MB, Rao SP, Barnes WS, Wintjens R, Walker JR,

423 Alonso S, Lee S, Kim J, Oh S, Oh T, Nehrbass U, Han SJ, No Z, Lee J, Brodin P, Cho SN, Nam K,
424 Kim J. 2013. Discovery of Q203, a potent clinical candidate for the treatment of tuberculosis. *Nature*
425 *medicine* **19**: 1157-1160. doi: 10.1038/nm.3262.
426 Pettersen EF, Goddard TD, Huang CC, Couch GS, Greenblatt DM, Meng EC, Ferrin TE. 2004.
427 UCSF Chimera--a visualization system for exploratory research and analysis. *Journal of*
428 *computational chemisty* **25**: 1605-1612. doi: 10.1002/jcc.20084.
429 Punjani A, Rubinstein JL, Fleet DJ, Brubaker MA. 2017. cryoSPARC: algorithms for rapid
430 unsupervised cryo-EM structure determination. *Nature Methods* **14**: 290-296. doi:
431 10.1038/nmeth.4169.
432 Rao SPS, Alonso S, Rand L, Dick T, Pethe K. 2008. The protonmotive force is required for
433 maintaining ATP homeostasis and viability of hypoxic, nonreplicating *Mycobacterium tuberculosis*.
434 *Proceedings of the National Academy of Sciences of the United States of America* **105**: 11945-11950.
435 doi: 10.1073/pnas.0711697105.
436 Rastogi N, Legrand E, Sola C. 2001. The mycobacteria: an introduction to nomenclature and
437 pathogenesis. *Revue Scientifique et Technique* **20**: 21-54. doi: 10.20506/rst.20.1.1265.
438 Rosenthal PB, Henderson R. 2003. Optimal determination of particle orientation, absolute hand, and
439 contrast loss in single-particle electron cryomicroscopy. *Journal of molecular biology* **333**: 721-745.
440 doi: 10.1016/j.jmb.2003.07.013.
441 Scherr N, Bieri R, Thomas SS, Chauffour A, Kalia NP, Schneide P, Ruf MT, Lamelas A,
442 Manimekalai MSS, Gruber G, Ishii N, Suzuki K, Tanner M, Moraski GC, Miller MJ, Witschel M,
443 Jarlier V, Pluschke G, Pethe K. 2018. Targeting the *Mycobacterium ulcerans* cytochrome bc_1:aa_3 for
444 the treatment of Buruli ulcer. *Nature communications* **9**: 5370. doi: 10.1038/s41467-018-07804-8.
445 Schrodinger LLC. 2010. *The PyMOL molecular graphics system, version 1.5. 0.4.* The PyMOL
446 molecular graphics system, version 1.5. 0.4.
447 Tortoli E, Fedrizzi T, Meehan CJ, Trovato A, Grottola A, Giacobazzi E, Serpini GF, Tagliazucchi S,

448 Fabio A, Bettua C, Bertorelli R, Frascaro F, De Sanctis V, Pecorari M, Jousson O, Segata N, Cirillo
449 DM. 2017. The new phylogeny of the genus Mycobacterium: The old and the news. *Infection,*
450 *Genetics and Evolution* **56**: 19-25. doi: 10.1016/j.meegid.2017.10.013.
451 Zheng SQ, Palovcak E, Armache JP, Verba KA, Cheng Y, Agard DA. 2017. MotionCor2: anisotropic
452 correction of beam-induced motion for improved cryo-electron microscopy. *Nature Methods* **14**:
453 331-332. doi: 10.1038/nmeth.4193.
454 Zivanov J, Nakane T, Scheres SHW. 2019. A Bayesian approach to beam-induced motion correction
455 in cryo-EM single-particle analysis. *IUCrJ* **6**: 5-17. doi: 10.1107/S205225251801463X.

456
457
458
459
460
461
462
463
464
465
466
467
468
469
470
471
472
473
474
475
476
477
478
479
480
481
482
483
484
485

Tables and Figures

		Strain	Query cover (%)	Ident (%)
Slowly growing mycobacteria	*Mycobacterium tuberculosis* complex	***Mycobacterium tuberculosis* complex**		
		Mycobacterium tuberculosis	100	100.00
		Mycobacterium africanum	87	99.79
		Mycobacterium bovis	99	87.46
		Mycobacterium canettii	100	99.82
		Mycobacterium microti	100	89.62
		Mycobacterium orygis	100	99.82
		Mycobacterium leprae	99	92.52
	Non-tuberculous mycobacteria	*Mycobacterium marinum*	99	88.71
		Mycobacterium ulcerans	99	88.89
		***Mycobacterium avium* complex**		
		Mycobacterium avium	99	88.53
		Mycobacterium intracellulare	99	86.92
		Mycobacterium chimaera	85	82.09
		Mycobacterium haemophilum	98	94.29
		Mycobacterium xenopi	99	89.96
		Mycobacterium kansasii	100	92.71
		Mycobacterium simiae	100	91.99
Rapidly growing mycobacteria		***Mycobacterium chelonae–abscessus* complex**		
		Mycobacterium abscessus subsp. abscessus	95	71.62
		Mycobacterium abscessus subsp. bolletii	94	78.23
		Mycobacterium chelonae	100	80.86
		Mycobacterium fortuitum	98	98.00

True pathogens Opportunistic pathogens

Figure 1. Sequences similarity comparison of *M. tuberculosis* QcrB with other pathogenic mycobacteria.

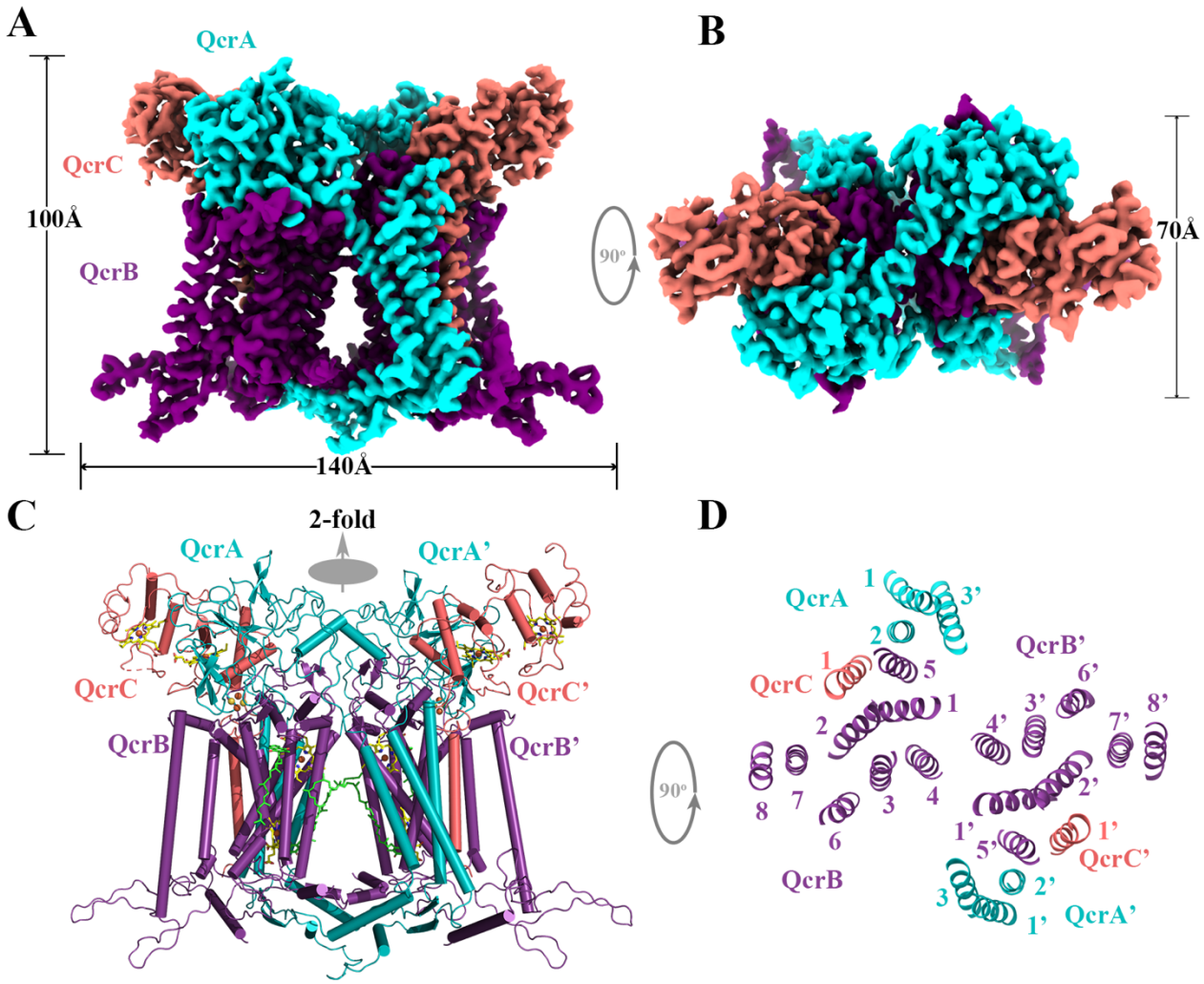

Figure 2. Overall architecture of the of *Mtb* cytochrome *bcc* complex. (**A**) Front view and (**B**) top view of cryo-EM map of cytochrome *bcc* at 2.68 Å resolution. QcrA, QcrB, and QcrC are colored teal, purple, and shalmon, respectively. (**C**) Cartoon representation of cytochrome *bcc*, using the same color scheme as above. The twofold symmetry of the dimer is depicted by the grey axis. The heme groups (b_H, b_L, c_{D1}, and c_{D2}) and menaquinone/menaquinol (MK_P/MK_N) are shown as stick models. The [2Fe-2S] clusters are shown as spheres. (**D**) A cross-sectional view (top) of cytochrome *bcc* dimer.

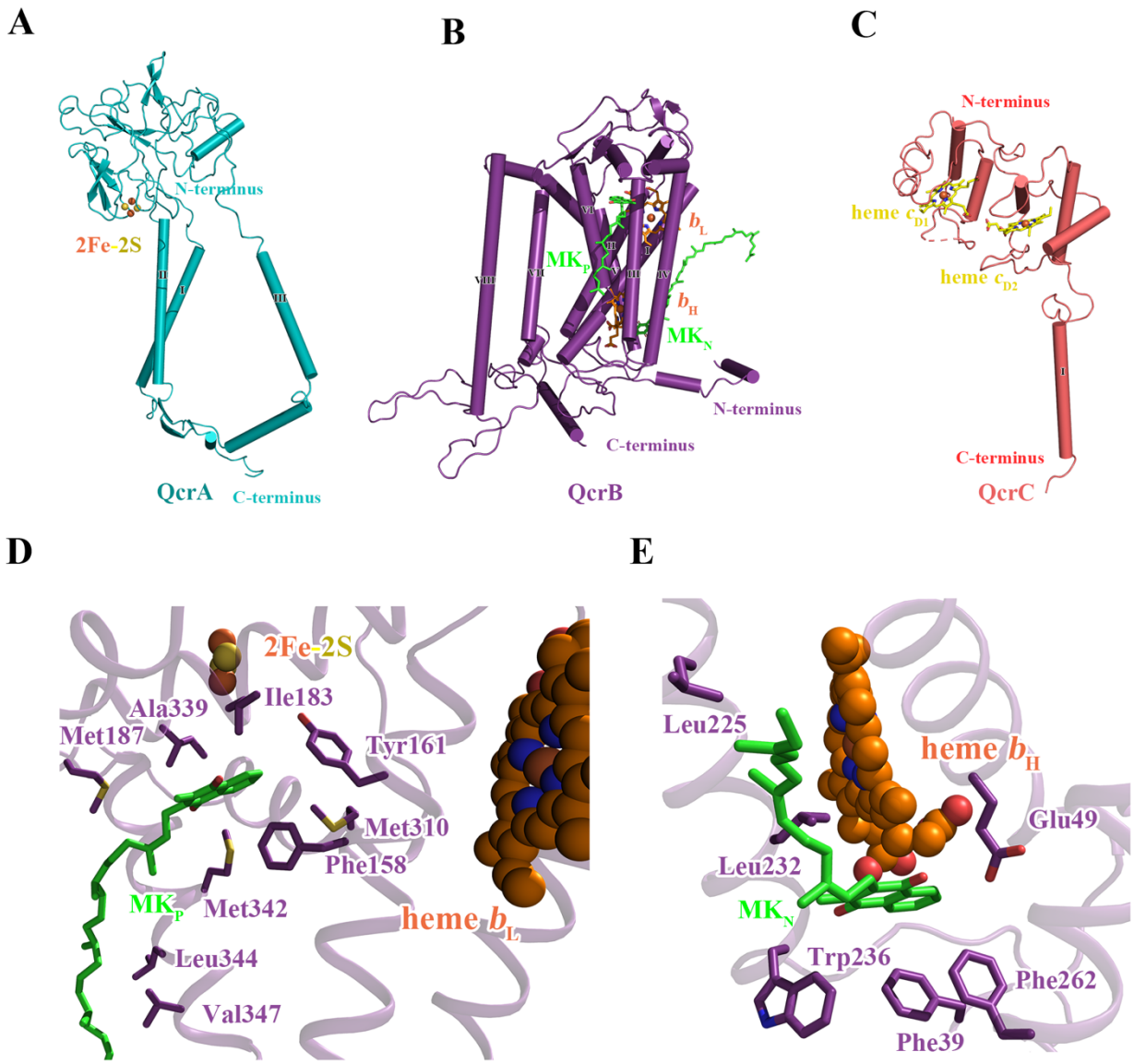

Figure 3. Structure of *Mtb* cytochrome *bcc* subunits. Cartoon representation of the monomers of (**A**) QcrA, (**B**) QcrB, and (**C**) QcrC, with prosthetic groups. (**D**) The Q_P binding site and (**E**) Q_N binding site. The residues potentially involved in the binding of MK/MKH_2 are shown with side chains in a stick representation. The MK/MKH_2 molecules are colored in green and shown as sticks. The [2Fe-2S] and heme groups are shown as spheres and labeled accordingly.

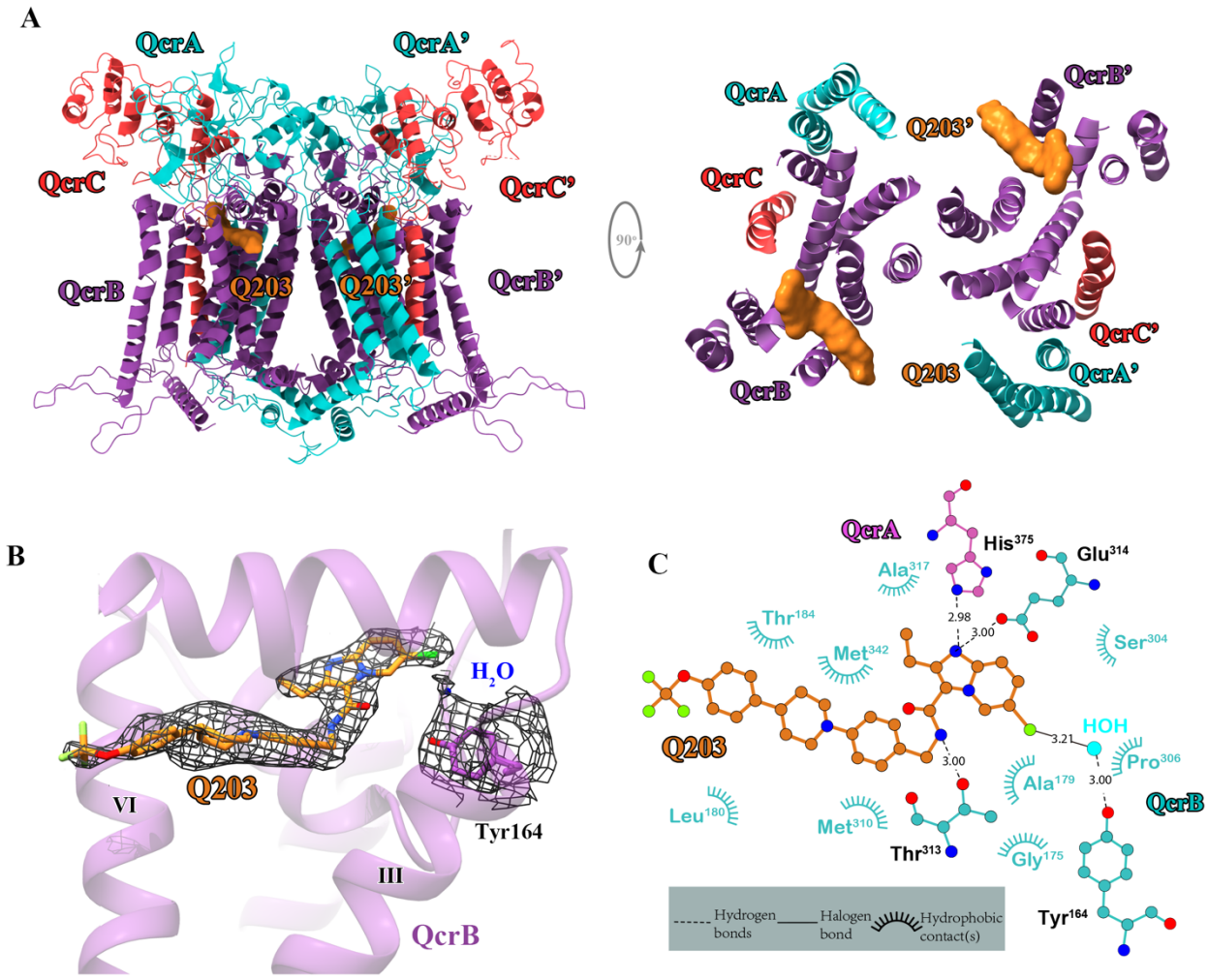

Figure 4. Cryo-EM structure of the *Mtb* cytochrome *bcc* complex in the presence of Q203. (**A**) Side (left) and top (right) views of the cryo-EM structure of the *Mtb* cytochrome *bcc* complex presented as a cartoon representation. Q203 (orange) is bound to the Qp site. (**B**) Visualization of densities for Q203, a water molecule and $_{QcrB}$Tyr164. (**C**) Plot of distances of various parts of Q203 to residues in the Qp site, determined using LIGPLOT (www.ebi.ac.uk/thornton-srv/software/LIGPLOT/).

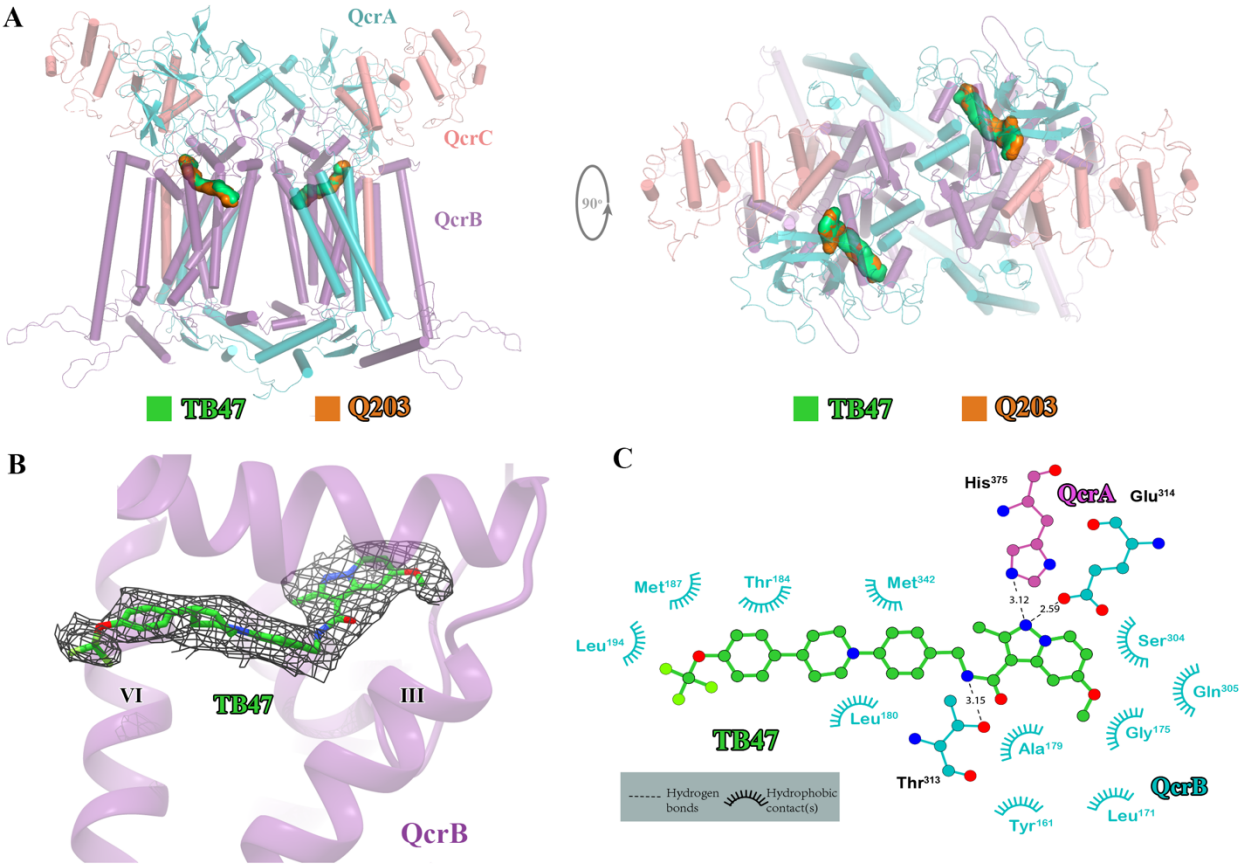

Figure 5. Cryo-EM structure of the *Mtb* cytochrome *bcc* complex in the presence of TB47. (**A**) Side (left) and top (right) views of the cryo-EM structure of the *Mtb* cytochrome *bcc* complex presented as a cartoon representation. The TB47 (green) and Q203 (orange) are bound to the Qp site. (**B**) Visualization of the density forTB47. (**C**) Plot of distances of various parts of TB47 to residues in the Qp site, determined using LIGPLOT (www.ebi.ac.uk/thornton-srv/software/LIGPLOT/).

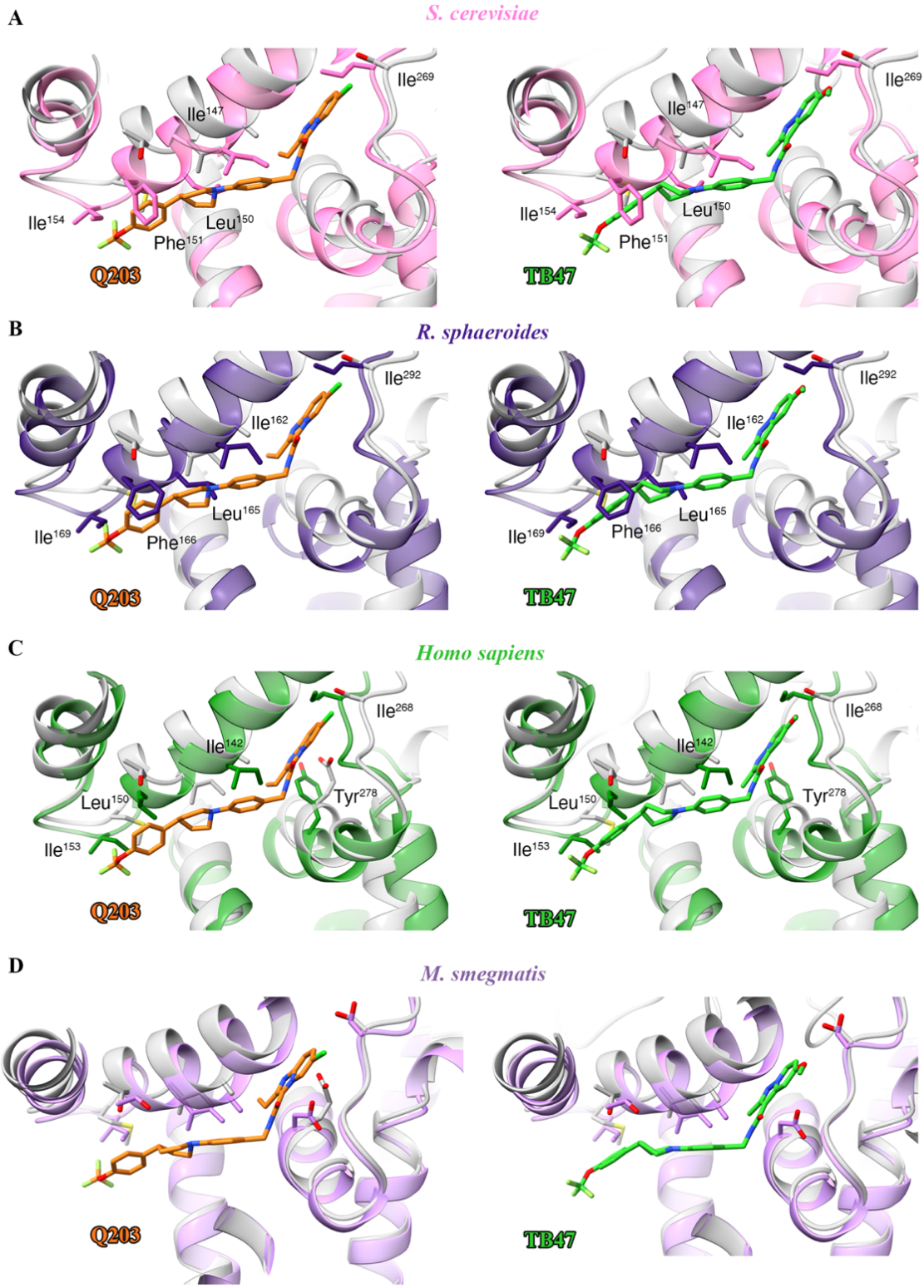

Figure 6. Structural alignment between the *Mtb* Qp binding pocket where Q203 or TB47 binds with homologous subunits from four other species. These subunits are from *S. cerevisiae* (pink, PDB: 1KYO), *R. sphaeroides* (blue, PDB: 2QJP), *Homo sapiens* (green; PDB: 5XTE), and *M. smegmatis* (violet, PDB: 6ADQ). Residues causing steric clashes in the homologous subunits are labeled. Q203 and TB47 are shown as orange and green stick models, respectively.

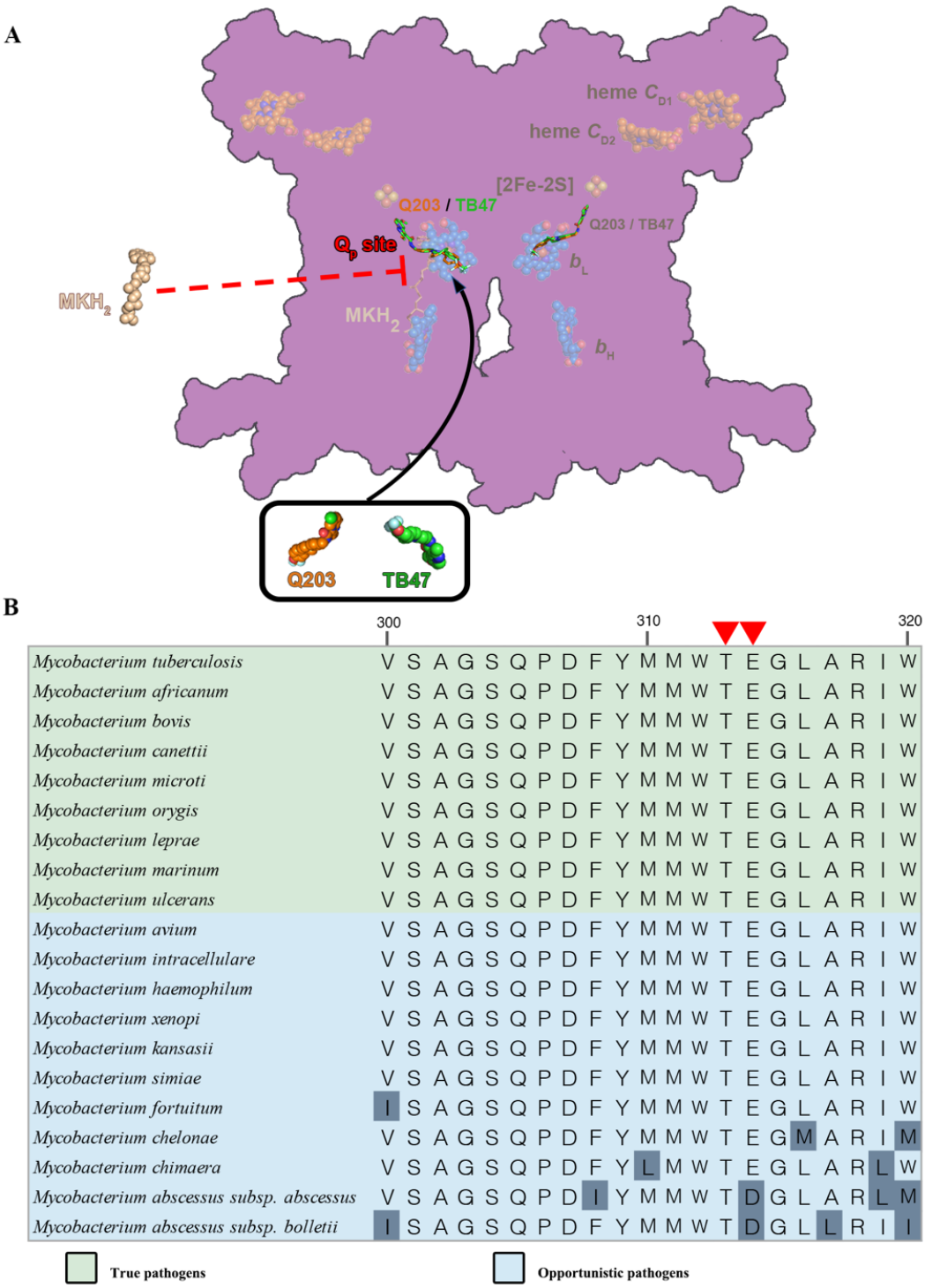

Figure 7. Proposed mechanism of inhibition and sequence alignment for the Q_P site within pathogenic mycobacteria. (**A**) Schematic of *M. tuberculosis* cytochrome *bcc* inhibition by Q203 and TB47. *M. tuberculosis* cytochrome *bcc* dimer are colored magenta. The binding of Q203 (orange spheres) or TB47 (green spheres) prevent substrate access (gray spheres). The prosthetic groups are shown in spheres and labeled accordingly. (**B**) Partial sequence alignment at the Qp site. The red triangles indicate the conservative residues involving with the hydrogen-bond formation between Q203 and TB47.

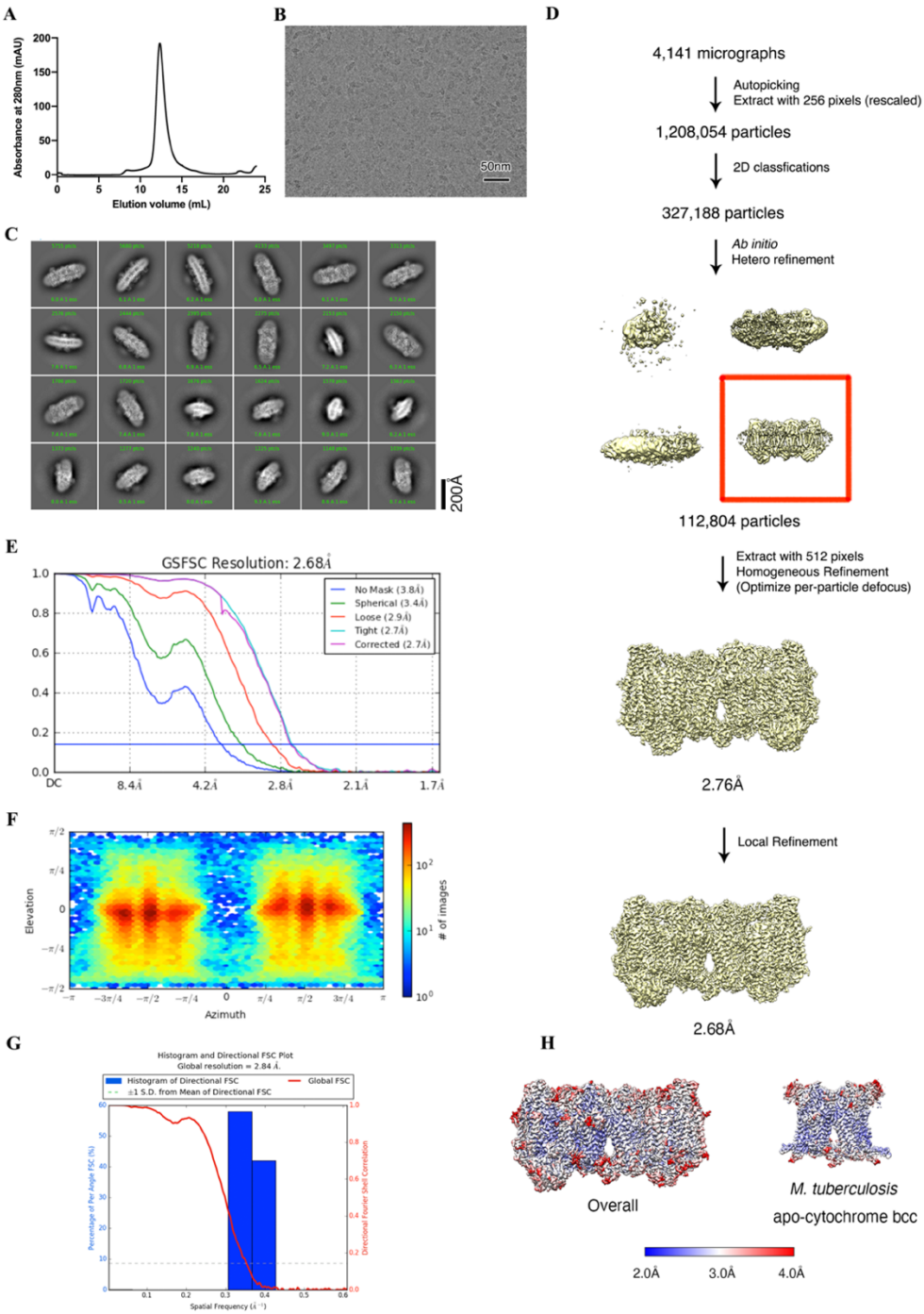

Figure 2-figure supplement 1. Cryo-EM data processing of apo hybrid supercomplex consisting of *Mtb* CIII and *Msm* CIV. (**A**) The elution profile of the *Mtb* cytochrome *bcc* from size exclusion chromatography (SEC). Peak fractions were pooled and concentrated for preparation on the cryo-EM grids. (**B**) Representative electron micrograph of the cryo-EM sample. (**C**)Representative 2D classification averages calculated from selected particles. (**D**) Workflow of data processing for the apo hybrid supercomplex. (**E**) FSC curves of 3D reconstructions. (**F**) Viewing direction of all particles used in the final 3D reconstruction. (**G**) 3DFSC histogram of final map. (**H**) The overall and *Mtb* cytochrome *bcc* maps, colored according to the local resolution.

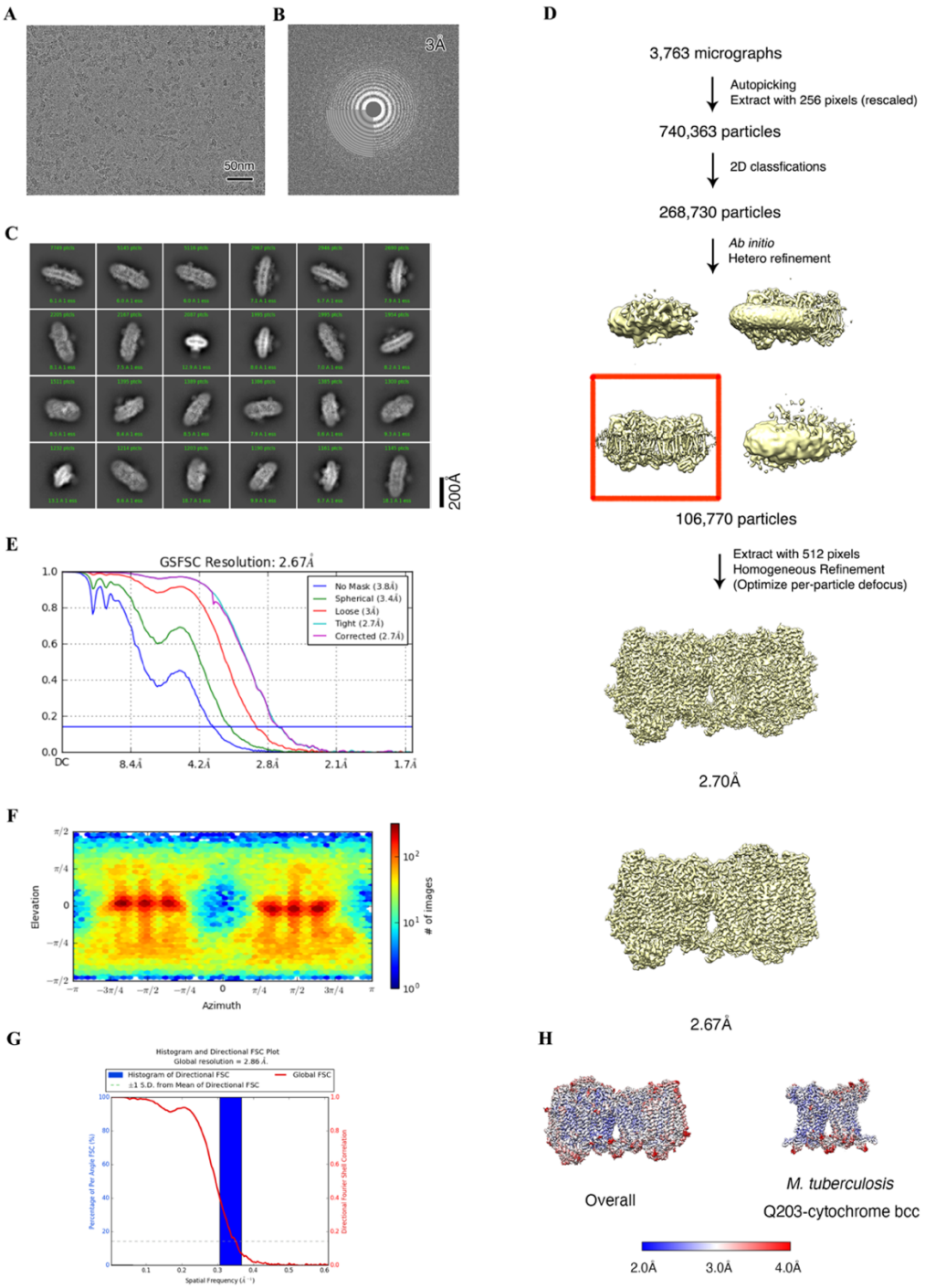

Figure 4-figure supplement 1. Cryo-EM data processing of hybrid supercomplex consisting of *Mtb* CIII and *Msm* CIV in the presence of Q203. (**A**) Representative electron micrograph of the cryo-EM sample. (**B**) CTF fit of motion-corrected micrographs (**C**) Representative 2D classification averages calculated from selected particles. (**D**) Workflow of data processing for the Q203-bound hybrid supercomplex. (**E**) FSC curves of 3D reconstructions. (**F**) Viewing direction of all particles used in the final 3D reconstruction. (**G**) 3DFSC histogram of final map. (**H**) The overall and *Mtb* cytochrome *bcc* maps, colored according to the local resolution.

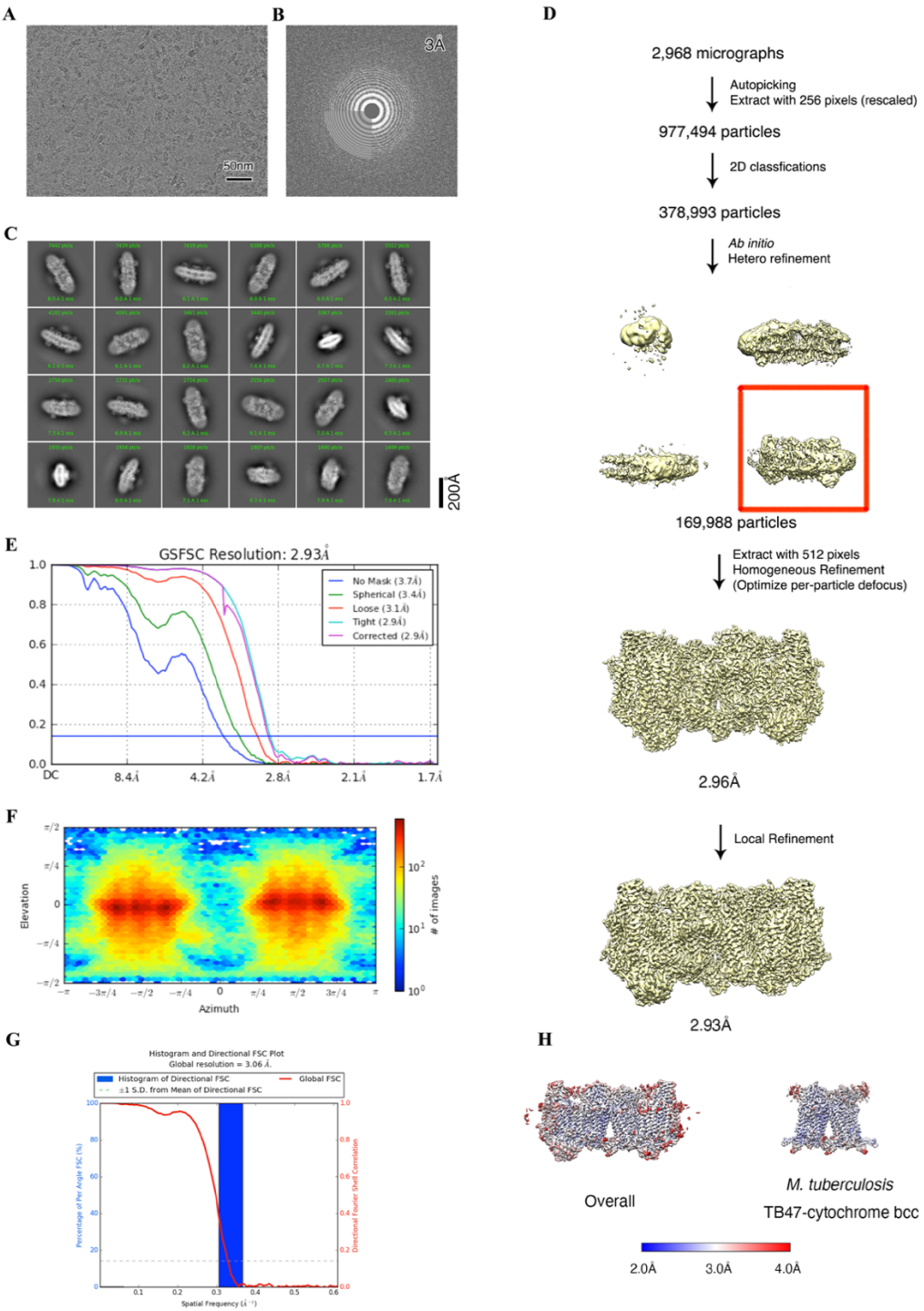

Figure 5-figure supplement 1. Cryo-EM data processing of the hybrid supercomplex consisting of *Mtb* CIII and *Msm* CIV in the presence of TB47. (**A**) Representative electron micrograph of the cryo-EM sample. (**B**) CTF fit of motion-corrected micrographs (**C**) Representative 2D classification averages calculated from selected particles. (**D**) Workflow of data processing for the TB47-bound hybrid supercomplex. (**E**) FSC curves of 3D reconstructions. (**F**) Viewing direction of all particles used in the final 3D reconstruction. (**G**) 3DFSC histogram of final map. (**H**) The overall and *Mtb* cytochrome *bcc* maps, colored according to the local resolution.

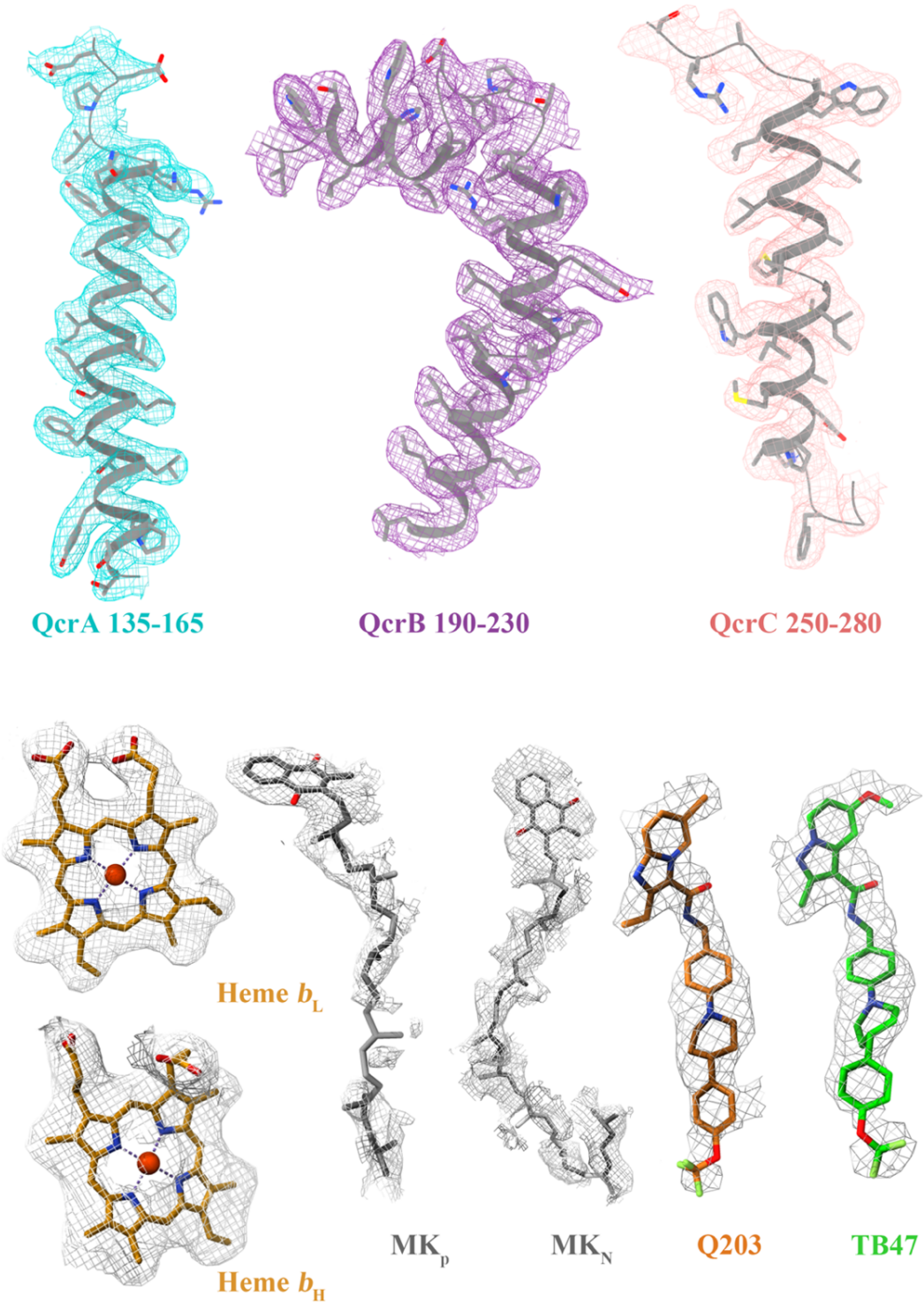

564

565 **Figures 2, 4, and 5-figure supplement 2. Cryo-EM map quality assessment and ligand**
566 **representation of *Mtb* cytochrome *bcc* complex.** Representative cryo-EM densities of individual
567 subunits, prosthetic groups and inhibitors. Corresponding subunits with residues, prosthetic groups
568 and inhibitors are shown in stick models or cartoon representation.

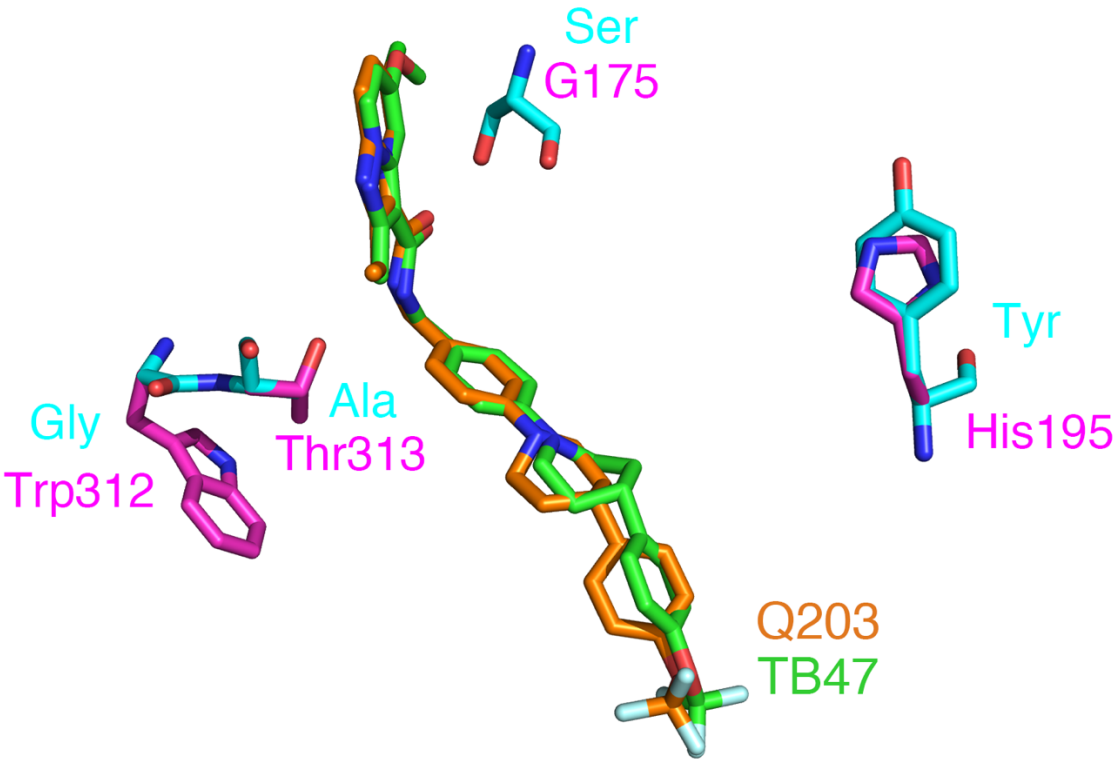

569
570 **Figures 4 and 5-figure supplement 3. Reported mutations in Q203- and TB47-resistant *M.***
571 ***tuberculosis.*** The native and mutant residues are colored magenta and cyan, respectively.
572

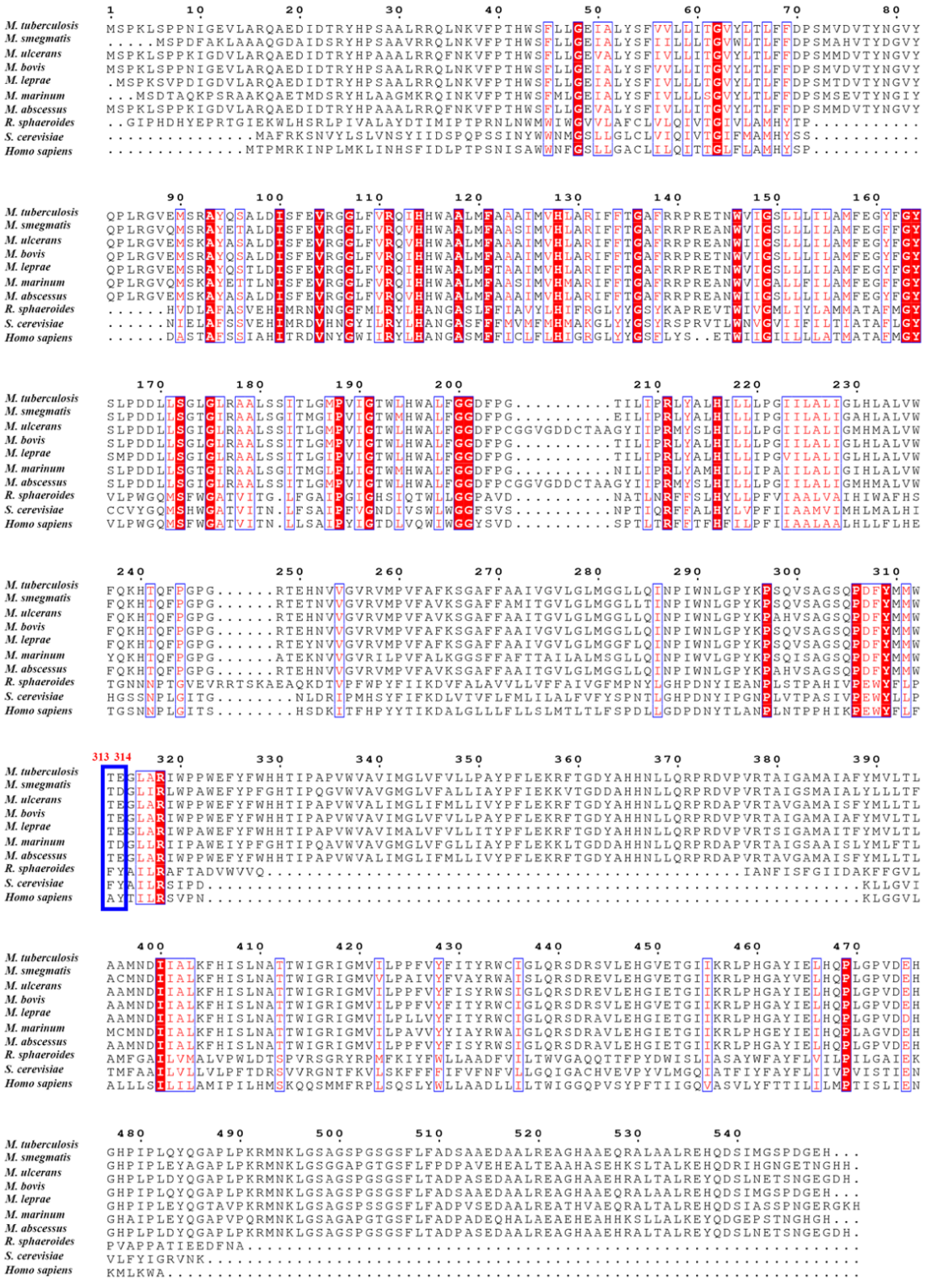

573

574 **Figure 6-figure supplement 1. Sequence alignment of *Mtb* QcrB with the counterparts in other**
575 **species and *Homo sapiens*.** Residues aligned to Thr313 and Glu314 are depicted in the thick blue
576 box. Red residues are conserved and blue indicates those less conserved.

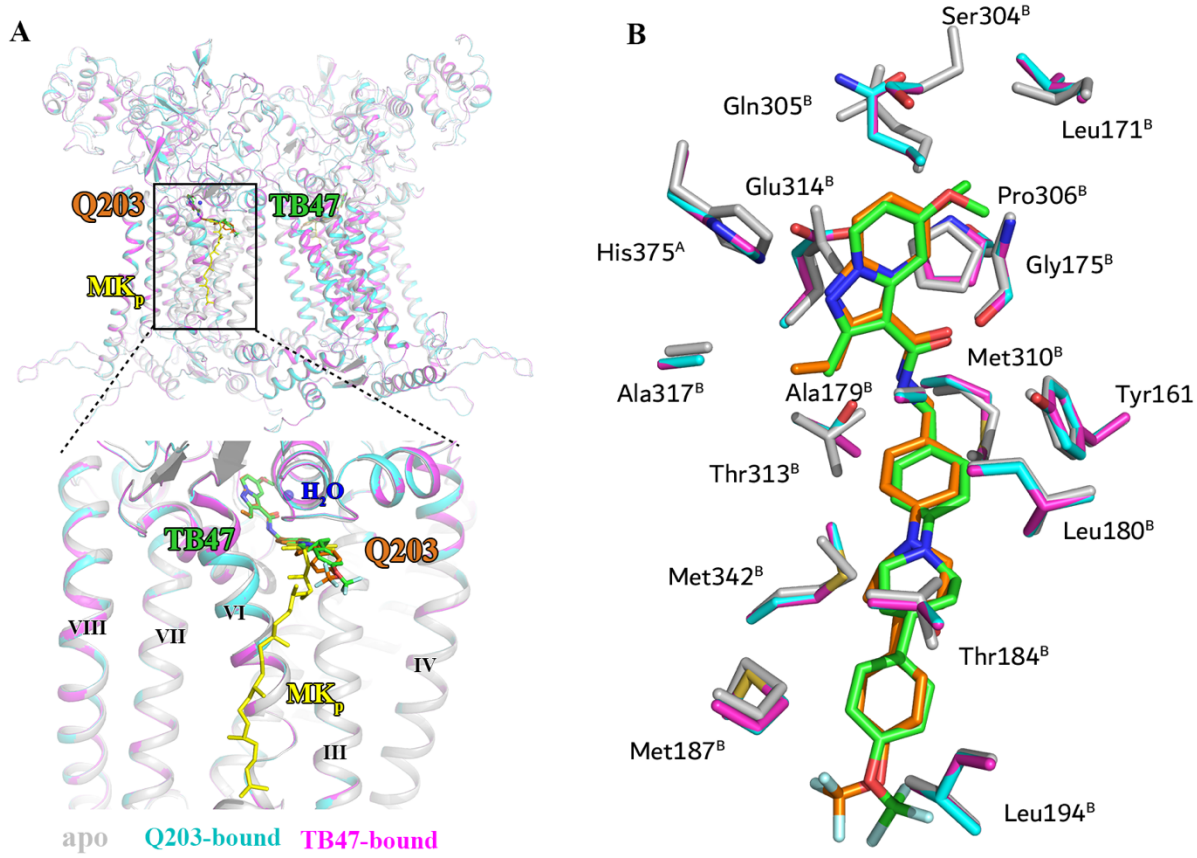

Figure 7-figure supplement 1. Comparison of apo and Q203/TB47-bound structures of *Mtb* cytochromes *bcc*. (**A**) Superposition of apo (gray), Q203-bound (cyan), and TB47-bound (magenta) structures of *Mtb* cytochromes *bcc*. The Q203 (orange), TB47 (green) and MK (yellow) molecules are shown as stick models, respectively. Water molecules are shown as spheres. The transmembrane helices are also labeled. (**B**) Comparison of residues surrounding Q203 (cyan sticks) and TB47 (magenta stick models) with those in apo form (gray sticks). The residues from subunits A and B are labeled with superscript A and B, respectively.

598 **Supplementary file 1. Cryo-EM data collection, refinement and validation statistics.**

Cryo-EM data collection, refinement and validation statistics			
State	**apo**	**Q203**	**TB47**
Data collection			
Microscope	Titan Krios	Titan Krios	Titan Krios
Voltage (kV)	300	300	300
Magnification	29,000x	29,000x	29,000x
Detector	Gatan K3	Gatan K3	Gatan K3
Data collection software	SerialEM	SerialEM	SerialEM
Electron exposure (e^{-}/Å^2)	60	60	60
Defocus range (μm)	-1.2 - -1.8	-1.2 - -1.8	-1.2 - -1.8
Pixel size (Å)	0.82	0.82	0.82
Data processing			
Number of micrographs	4,141	3,763	2,698
Final particle images	112,804	106,770	169,988
Symmetry imposed	C1	C1	C1
Map resolution (Å)			
FSC 0.143 threshold	2.68	2.67	2.93
Refinement			
Initial model used (PDB code)	6ADQ	-	-
Map sharpening B factor (Å^2)	- 65.3	-70.0	-97.5
d FSC model (0.143) Masked	2.5	2.6	2.9
Map correlation coefficient	0.89	0.88	0.90
Mean CC for ligands	0.78	0.76	0.79
Model composition			
Non-hydrogen atoms	42,281	42,960	42,625
Protein residues	5,122	5,132	5,119
Ligands			
	9Y0: 2	9Y0: 3	9Y0: 2
	CDL: 17	CDL: 17	CDL: 17
	9YF: 4	9YF: 6	9YF: 6
	HEA: 4	HEA: 4	HEA: 4

	HEC: 4 MQ9: 10 HEM: 4 PLM: 4 CU: 8 FES: 2	HEC: 4 MQ9: 8 HEM: 4 PLM: 4 CU: 8 FES: 2 HUU: 2 9XX: 2	HEC: 4 MQ9:8 HEM: 4 PLM: 4 CU: 8 FES: 2 HV0: 2
R.M.S. deviations			
Bond lengths (Å)	0.005	0.003	0.005
Bond angles (°)	1.057	0.659	0.739
Validation			
MolProbity score	1.86	1.84	1.87
Clashscore	7.26	7.20	7.17
Poor rotamers (%)	0.05	0.10	0.10
Ramachandran plot			
Favored (%)	92.76	93.07	92.39
Allowed (%)	6.97	6.61	7.25
Outliers (%)	0.28	0.31	0.36
Cβ outliers (%)	0.00	0.00	0.00

599